AIAA 2008-1102

46th AIAA Aerospace Sciences Meeting and Exhibit, 7-10 Jan 2008, Reno, Nevada

Flow control on a three dimensional forebody using pulsed dc plasma actuator operating in air

K.P. Singh* and Subrata Roy†

Computational Plasma Dynamics Laboratory and Test Facility
Mechanical and Aerospace Engineering, University of Florida
Gainesville, FL 32611-6300, USA

A pulsed dc plasma actuator can be used as an alternate to dielectric barrier discharge plasma actuator. The effect of such pulsed dc plasma actuators operating in oxygen gas is studied using a self-consistent multibody system of neutral oxygen species and plasma. The equations governing the motion of charged species are solved with drift diffusion approximation. The space electrostatic potential is computed from the Poisson's equation. The highest electric field and ionization levels are close to the junction of electrodes and dielectric. The time average of the force shows mostly acceleration in the forward direction (from anode to cathode) above the actuator.

Nomenclature

D	Diffusion coefficient, cm^2/s	O	Oxygen atom
E	Electric field, V/cm	O_2^+	Positive oxygen ion
e	Electron charge, coulomb	O^-	Negative oxygen ion
ε	Permittivity, farad/m	P	Pressure, Pa
F	Electric force density, dynes/cm^3, $\mu N/cm^3$	*t*	Time coordinate, s
F	frequency	T	Temperature, eV
ϕ	Potential, V	**V**	Velocity, m/s
K	Rate coefficients, $cm^3\,s^{-1}$	*x,y,z*	Spatial coordinate, cm
k_B	Boltzmann constant		
L	Electrode length, cm	Subscripts:	
λ_D	Electron Debye length, cm	α	Species
M	mass, kg	B	Boltzmann
μ	Mobility, $cm^2V^{-1}s^{-1}$	*e*	Electron, finite element
n	Number density, cm^{-3}	*i*	Ion
O_2	Oxygen molecule	*n*	Neutral

I. Introduction

FLIGHT vehicle forebody vortex symmetry breaking and control of resulting yaw departure by active and passive means have been studied by many researchers. Such study includes numerical simulation, analytical interpretation and experiments. [1-6] For example, flow control using flow injection and surface heating has been investigated for asymmetric flows around circular cones by using computational solution of the unsteady, compressible full Navier-Stokes equations.[1] Passive vortical flow control on a wing-body combination using tangential blowing has also been studied.[2] The feasibility of using forebody tangential blowing to control the roll-yaw motion of a wind-tunnel model at high angles of attack has been shown experimentally.[3] Analytical modeling for a circular cone for determining the stability of point vortices to small symmetric and asymmetric displacements were qualitatively validated against experimental results.[4]

* Post Doctoral Research Associate of the CPDLT, AIAA Senior Member.
† Associate Professor, Mechanical and Aerospace Engineering, 336 MAE-B, PO Box 116300, AIAA Associate Fellow.

As an alternative to blowing, surface discharge plasmas may be employed to actively control or eliminate vortical asymmetry about the nose of a conical forebody at an angle of incidence. In recent years, both dc and ac plasma actuators have demonstrated the ability to control separation on airfoils at a high angle-of-attack.[7-10] The plasma actuator can be used to increase the lift and/or reducing the drag of airfoils and fuselages through electrodynamic force. It has been shown by the experiments[7-9] and simulations[10-12] that the plasma actuator imparts momentum to the boundary layer inducing rapid flow attachment. High-frequency spark discharge plasma was used to control asymmetric vortical structures on the conical forebody.[5] Results of wind tunnel experiments show that plasma actuators distributed near flow separation lines may be used for successful control or elimination of vortex asymmetry. A detailed two dimensional theoretical study for flow control over a conical section was reported using a single barrier discharge actuator and a set of dc plasma actuators.[6] Results show insufficient control of the flow on the entire length of the forebody due to a single barrier discharge actuator. Flow control on the conical forebody cross-section using several pulsed dc plasma actuators show considerable improvement for separated neutral gas flow at 17.5 deg angle of attack.

The plasma may operate under a Townsend avalanche and a glow discharge. The V-dot probe technique shows that the voltage across the plasma is less than half of that which is applied across the electrodes [13] in a large vacuum chamber and a linear relationship between the force production and air pressure was found during experimental measurements of the force of a plasma actuator [14]. The airflow was found to have a significant influence on the plasma characteristics during an investigation of different airflow velocities, plasma excitation frequencies and voltages [15]. The body force was found to be proportional to frequency for a constant voltage. The body force increases with voltage for a constant frequency [16]. The induced jet velocity depends on the applied voltage and frequency [17-18]. The actuator power can be reduced by 90 percent and its durability can be improved by operating it in an unsteady manner [19].

Plasma actuator was also treated as a heat and momentum input into a small control volume [8]. Reported measurements indicate that the momentum coupling between the charged particles and the neutral particles occurs on timescales much shorter than that for the bulk fluid motion. A detailed numerical model of plasma with eight species air chemistry with nitrogen and oxygen mixture has found effect of different charged species into the generation of electrodynamic force that controls flow of the surrounding fluid [20]. However, the influence of plasma actuators are limited by different kinds of power losses such as reactive power losses due to impedance mismatch between the power supply and the actuator, dielectric heating, plasma joule heating which need to be minimized for optimum performance [6,21,22].

As an extension of our two dimensional model [6,20], in this paper we present the results of the flow control on a three-dimensional conical forebody using pulsed dc plasma actuator operating in weakly ionized oxygen gas. The section II gives geometry description and the section III gives details of oxygen chemistry. The fourth section provides details of initial and boundary conditions. The response to the applied pulsed dc potential is described in section V. Conclusions are drawn in the final Section VI.

II. Geometry Description

Fig. 1 shows schematic of a pulsed dc plasma actuator. The simulated region is 60^o segment of a cone. The segment extents from z=0.06 cm to z=4.0 cm. The surface containing the electrodes and dielectric is given by $x = 0.16\sin(360-\alpha)$ cm to $x = 0.5\sin(360-\alpha)$ cm and $y = 0.16\cos(360-\alpha)$ cm to $y = 0.5\cos(360-\alpha)$ cm, where α varies from 0^o to 60^o. The domain of simulation consists of a 2 mm thick air packet coating over this curved surface. The pulsed dc plasma actuator consists of four electrodes separated by a dielectric. The powered electrodes are marked by P and grounded electrodes by G the Figure 1. The electrodes are exposed to the air. Thickness of each electrode is 2.0 mm along the z-direction. The powered and grounded electrodes are separated by dielectric. Thickness of dielectric separating the electrodes is 2.0 mm along the z-direction. The powered electrodes are from z=1.6 cm to z=1.8 cm and z=2.4 to z=2.6 cm. The dielectric surface between the electrodes is from z=1.8 cm to z=2.0 cm, z=2.2 cm to z=2.4 cm and z=2.6 cm to z=2.8 cm. The grounded electrode is from with z=2.0 cm to z=2.2 cm and z=2.8 to z=3.0 cm. We have chosen the relative dielectric constant ε_r = 10. The domain is filled with air of relative dielectric constant ε_r = 1.0055. The height of the electrodes is assumed negligible. A pulsed dc voltage of $\phi = \phi_0 \sin^4(2\pi ft)$ volts is applied to the powered electrode. We have chosen with ϕ_0=1000 volt, and f = 5 kHz.

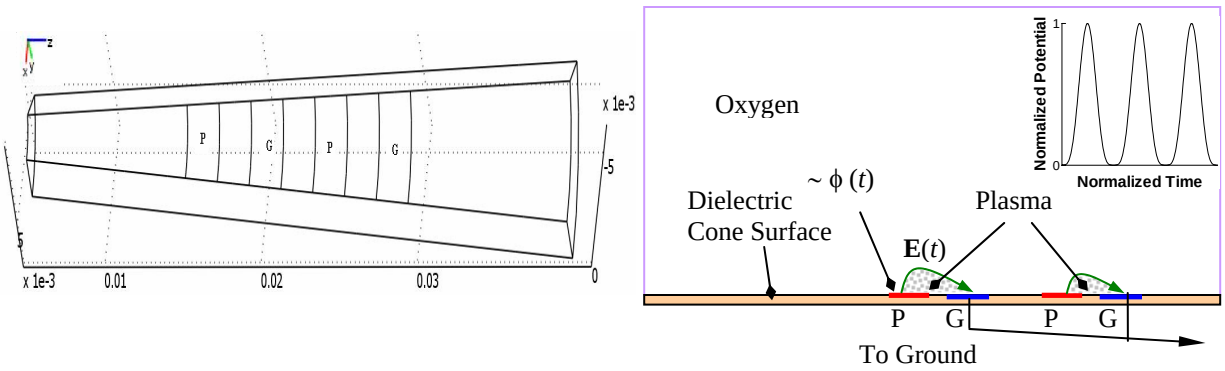

Figure 1. Schematic of asymmetric single dielectric barrier plasma actuators operating in oxygen gas.

III. Oxygen Chemistry

For the oxygen chemistry we neglect the metastable species along with O^{4+} due to their extremely high recombination rates. O_2^- is not included in this paper due to the reason explained at the end of Section V. Also, the numerical complexity is further simplified by excluding nitrogen chemistry at this stage. The model equations governing chemistry of discharge are as follows.[23]

(a) Ionization $e + O_2 \rightarrow O_2^+ + 2e$, (1a)

(b) Dissociation $e + O_2 \rightarrow 2O + e$, (1b)

(c) Dissociative attachment $e + O_2 \rightarrow O_- + O$, (1c)

(d) Recombination $O^- + O_2^+ \rightarrow O + O_2$, (1d)

(e) Dissociative recombination $O + O^- \rightarrow O_2 + e$, (1e)

The drift-diffusion form of continuity and Poisson equations for the electrons, ions and neutrals are as follows:

$$\frac{\partial n_e}{\partial t} + \nabla.(n_e \mathbf{v}_e) = (k_1 - k_3) n_e n_{O_2} + k_5 n_O n_{O^-} \quad (2)$$

$$\frac{\partial n_{O_2}}{\partial t} + \nabla.(n_{O_2} \mathbf{v}_{O_2}) = -(k_1 + k_2 + k_3) n_{O_2} n_e + k_4 n_{O^-} n_{O_2^+} + k_5 n_O n_{O^-} \quad (3)$$

$$\frac{\partial n_O}{\partial t} + \nabla.(n_O \mathbf{v}_O) = (2k_2 + k_3) n_e n_{O_2} + k_4 n_{O^-} n_{O_2^+} - k_5 n_O n_{O^-} \quad (4)$$

$$\frac{\partial n_{O^-}}{\partial t} + \nabla.(n_{O^-} \mathbf{v}_{O^-}) = k_3 n_e n_{O_2} - k_4 n_{O^-} n_{O_2^+} - k_5 n_O n_{O^-} \quad (5)$$

$$\frac{\partial n_{O_2^+}}{\partial t} + \nabla.(n_{O_2^+} \mathbf{v}_{O_2^+}) = k_1 n_e n_{O_2} - k_4 n_{O^-} n_{O_2^+} \quad (6)$$

$$\nabla \bullet (\varepsilon \nabla \phi) = e(n_e + n_{O^-} - n_{O_2^+}), \quad (7)$$

Above the momentum flux $n_\alpha \mathbf{v}_\alpha = -\mathrm{sgn}(e) n_\alpha \mu_\alpha \nabla\phi - D_\alpha \nabla n_\alpha$, (8)

and the electric field $\mathbf{E} = -\nabla\phi$. (9)

The electron temperature is calculated from $\mathbf{E} = k_B T_e/(\nabla n_e/n_e)$, which is obtained assuming an initial Boltzmann distribution, $n_e \propto \exp(e\phi/k_B T_e)$. Various rate coefficients k_1, k_2,…k_5 related to in Eqs. (1a) through (1e) are obtained [23] as functions of electron temperature. The secondary electron emission from the exposed surface is taken as a function of incident electron energy[24] and remains small, i.e., less than 10^{-3}. No material sputtering of the surface is considered. In Eqns. (2)-(7), n_α and $\mathbf{v}_\alpha$ are density and velocities of species α. The mobilities μ_α and diffusion rates D_α are given [25]. The bulk density of the oxygen is taken to be 0.35 kg/m^3 at atmospheric pressure.

IV. Numerical Model

Initial and boundary conditions are as follows. The all initial particle concentrations, except those of the electrons, and oxygen molecules, are taken zero. Initial atmospheric oxygen molecule density is taken as $10^{26}/m^{3,}$ and the electron density is taken as $10^{9}/m^{3}$. Initial pulsed dc potential is zero. These initial conditions have been chosen to match with the realistic atmospheric conditions.

The boundary conditions for the Poisson's equation are as follows: The potential difference with ϕ_0 = 1000 volt is applied to the first electrode of the pair. The other electrode of the pair is grounded. The powered electrodes are marked by **P** and grounded electrodes by **G** the Figure 1. The powered and grounded electrodes are separated by dielectric. Electric insulation condition (normal component of electric field equal to zero) is assumed at outer boundaries of the domain and at the dielectric surface.

Boundary conditions related to oxygen species continuity equations are as follows: the currents flow normal only to the rf electrode since it is an equipotential surface. Homogeneous Neumann conditions are applied to the outer edges of the domain and electric insulation is assumed at the surface of the dielectric. The normal currents at the surface of dielectric are taken zero.

The ionized oxygen gas is numerically modeled using a self-consistent three-dimensional Galerkin variational formulation based finite-element method[20] to obtain electron, ion and neutral species densities of oxygen, and the electric potential distribution. Finite element techniques are well known for their adaptability to arbitrary multidimensional geometries and accurate imposition of complicated boundary conditions. Here, the equation sets (1): (9) can be written with operator L as L (**U**) = 0 where **U** contains state variables like species number densities and potential. Multiplying with a permissible test function η and integrating over the spatially discretized domain Ω, the variational statement results in the weak form

$$WS^h = \Im_e \left(\int_{\Omega_e} \left[\eta L(\mathbf{U}) d\tau \right] \right)_e = 0 \tag{10}$$

for a discretization h of $\Omega = \bigcup \Omega_e$ and $\Im_e$ is the non-overlapping sum over the elements. Application of Green-Gauss divergence theorem "weakens" the order of derivatives in (10) and yields natural homogenous Neumann boundary conditions. The surface integral thus resulting in Eqn. (10) contains the (un)known boundary fluxes wherever fixed or flux boundary conditions are enforced accurately. Thus, for example, the Galerkin form of Eqn. (7) becomes,

$$\sum_e \left(\int_{\Omega_e} \frac{d\eta}{dz} \varepsilon \frac{d\eta^T}{dz} dz \{\phi\}_e + e \int_{\Omega_e} \eta \eta^T dz \{n_e\}_e - e \int_{\Omega_e} \eta \eta^T dz \{n_{O_2^+}\}_e + e \int_{\Omega_e} \eta \eta^T dz \{n_{O^-}\}_e - \int_{\Omega_e \cap \partial\Omega_e} \eta \varepsilon \frac{d\eta^T}{dz} dz \{\phi\}_e = F_\phi \right)_e \tag{11}$$

where F_ϕ is the solution residual.

The Jacobian matrix J=[$\partial F/\partial$**U**] in the global $[J].\{\partial \mathbf{U}\} = -\{F\}$ is resolved using LU-decomposition scheme for updating change in discretized solution vector **U** at each iteration. The terminal non-linear ordinary differential equation (ODE) systems are solved using implicit Euler method for temporal evolution and N-R iterative algorithm for the non-linear matrix algebra. The convergence criterion for all variables at any iteration is set at 10^{-4}. Solution stability is ensured by appropriate selection of adaptive time marching step size and the introduction of artificial diffusion.

Independent of the physical dimension of the working domain Ω, and for general forms of the flux vectors, the semi-discretized weak statement always yields an ordinary differential equation (ODE) system that is *fully discretised* using a θ-implicit or τ-step Runge-Kutta type time integration. The terminal ODE is usually solved using a Newton-Raphson scheme for **U**(t):

$$\begin{aligned} \mathbf{U}_{\tau+1}^{i+1} &= \mathbf{U}_{\tau+1}^{i} + \Delta\mathbf{U}^i = \mathbf{U}_\tau + \sum_{p=0}^{i} \mathbf{U}^{p+1}, \text{ where} \\ \Delta\mathbf{U}^i &= -\left[\mathbf{M} + \theta\Delta t(\partial\mathbf{R}/\partial\mathbf{U})\right]^{-1} \mathbf{R}(\mathbf{U}) \end{aligned} \tag{12}$$

Here, a θ–implicit time marching procedure is employed. In (12), **M** = S_e(**M**$_e$) is the "mass" matrix associated with element level interpolation, **R** carries the element convection, diffusion and source information. The calculation of the "Jacobian" ∂**R**/∂**U** and inversion of the **M**+$\theta\Delta t(\partial\mathbf{R}/\partial\mathbf{U})$ matrix with sufficient accuracy is obviously a numerical challenge. However, unlike the traditional finite difference/volume methods, the present FE algorithm allows one to simulate the system simultaneously without requiring any sub-iteration for the Poisson solver.

V. Results and Discussion

Discharge starts in the oxygen as we switch on the pulsed dc voltage. Different ion and neutral species are formed through ionization, dissociation and dissociative attachment etc. Recombination also occurs. Full chemistry of different species formation and recombination is described by Equation (1). The simulation results at the peak of the 10th cycle of the pulsed dc are given in Figures 2-6.

Figure 2(a) and 2(b) show electric potential and electric field components as a function of z at α = 15° and 45° for a pulsed dc plasma actuator. As mentioned earlier that very first electrode from the left is powered electrode. Then there is dielectric of 2 mm thickness and then a grounded electrode. The sequence is repeated for second set of electrodes and dielectric. The variation of various components of electric field on the surface follows from applied of electric potential. Electric field is given by $\mathbf{E} = -\nabla\phi$. Since the gradient of electric field is highest at the edges the electrodes, the value of electric field is highest there. The potential does not change with z for the powered and grounded electrodes. The gradient of electric potential with respect to z is zero. The value of E_z is zero at the electrodes surfaces. The potential is not constant with respect to x or y, hence E_x and E_y are not zero at the electrode surfaces. The curvature of the electrodes with lower values of z is high; the electric field is high for these electrodes. Higher ionization occurs for these electrodes.

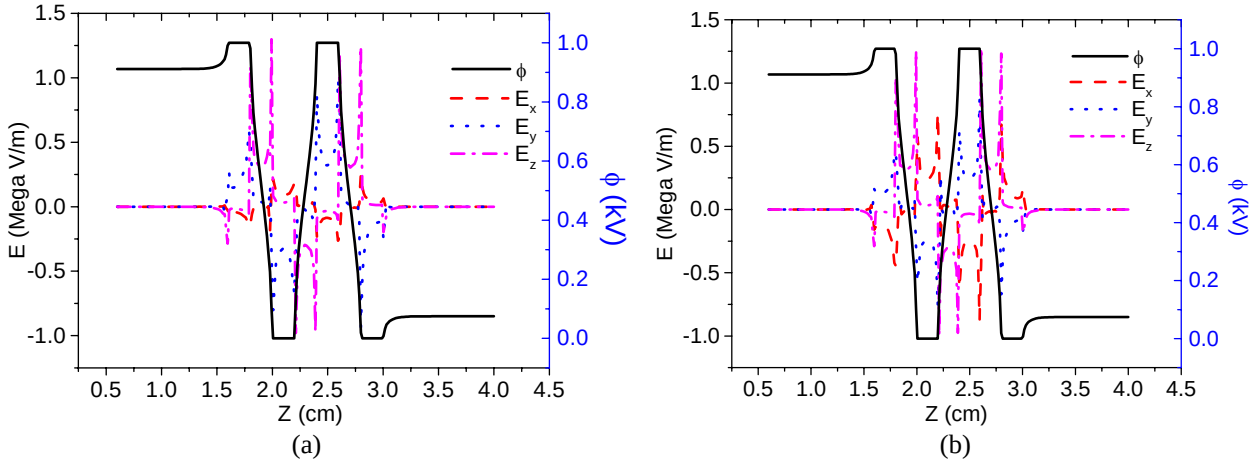

Figure 2. Electric potential and electric field components as a function of z at (a) α = 15 deg and (b) α = 45 deg.

Figures 3 (a) shows spatial distribution of electron density for pulsed dc plasma actuator. Chemistry of electrons formation is given by set of Equations (1a). Spatial and temporal density profile of electrons is governed by continuity Equation (2) coupled with other equations. Electron density rises up to a level 4 $\times 10^{14}/m^3$. Electrons respond to electric field very fast due to low mass and high mobility. The electrons are repelled from the area of grounded electrode and are attracted towards rf electrode where they are lost. Figure 4 (a) shows slices of density of electrons at the positive peak of the pulsed dc of tenth cycle. The density decreases sharply with the increase in the distance from the surface of the electrodes and dielectric.

The oxygen ions O^- are produced through dissociative attachment of oxygen molecules with electrons governed by the Eqn. (1c). Its density is governed by continuity Eqn. (5) coupled with other equations. The density of oxygen ions O^- grows to a level of nearly 3 $\times 10^{15}/m^3$. Figure 3 (b) shows density profile of negative oxygen ions O^- at positive peak of the pulsed dc of tenth cycle. The negative oxygen ions play an important role in oxygen chemistry. The oxygen ions O^- are repelled from the area of grounded electrode and are attracted towards powered electrode under the influence of pulsed dc. At the electrode oxygen ions O^- become a part of normal current. The oxygen ions O^- are much heavier than that of electrons and its mobility is low; response is slow.

The edge of the powered electrode is at z=1.8 cm. The peak of density is close to the edge of the powered electrode. Electric field is highest at the edges hence higher ionization occurs at these locations. The curvature of the electrodes at lower values of z is higher. The electric field is higher for higher curvature. This increases ionization for the electrodes with lower values of z. Figure 4 (b) shows slices of density of negative oxygen ions O^- at positive peak of the pulsed dc of tenth cycle at electrode edges. The density decreases sharply with the increase in the distance from the edge of the electrodes or dielectric.

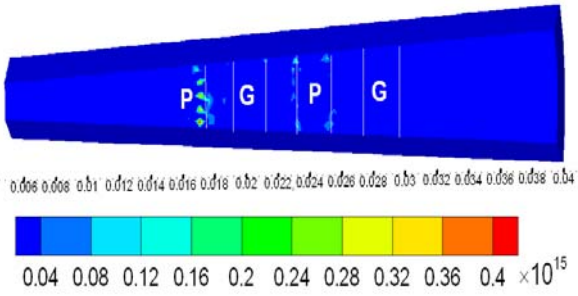

(a) electron density

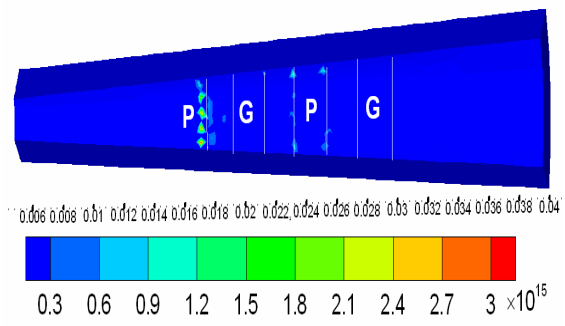

(b) O- density

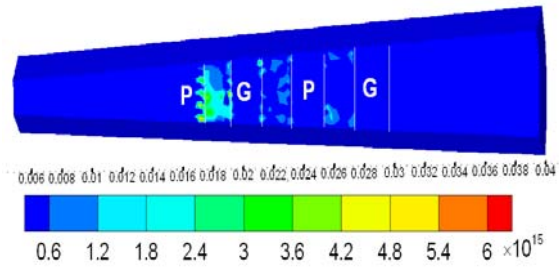

(c) O+ density

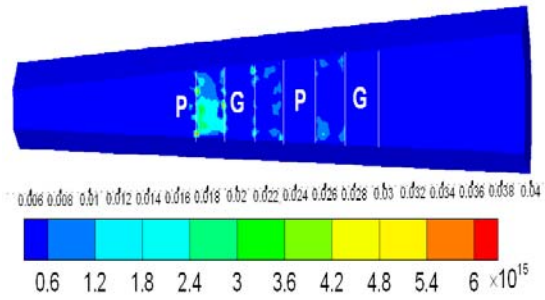

(d) charge density

Figure 3. Surface plot of density (m^{-3}) of (a) electrons, (b) negative oxygen ions O^-, (c) positive oxygen ions O_2^+ and (d) separated charge density $n_q = n_{O_2^+} - n_e - n_{O^-}$.

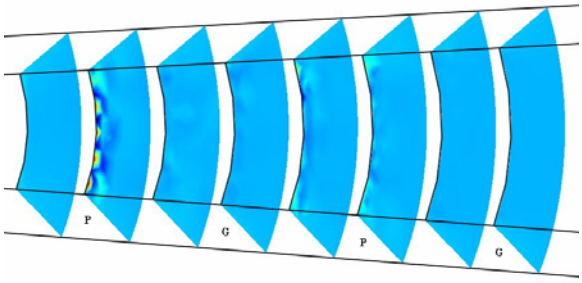

(a) electron density

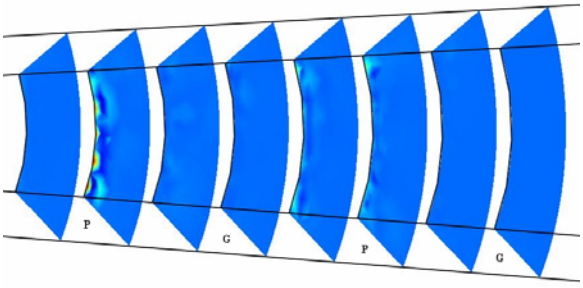

(b) O^- density

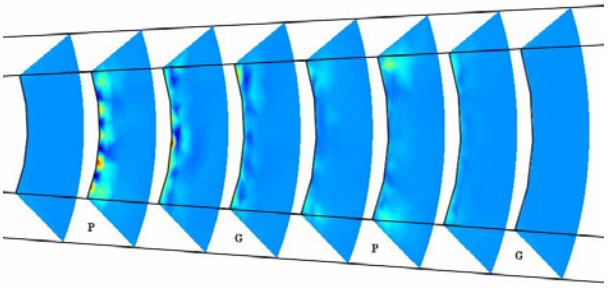

(c) O_2^+ density

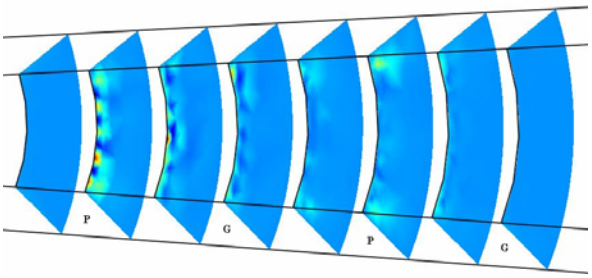

(d) charge density

Figure 4. Slices of density (in m^{-3}) contours at edges of electrodes of (a) electrons, (b) negative oxygen ions O^-, (c) positive oxygen ions O_2^+ and (d) separated charge density $n_q = n_{O_2^+} - n_e - n_{O^-}$.

Response of negative species to the electric field is opposite to that of positive ions. Ion mass and motilities are also different for different oxygen species and electrons, hence, their velocities are different. This gives rise to charge separation given by $n_q = n_{O_2^+} - n_e - n_{O^-}$. Figure 3 (d) shows density profile of charge separation at positive peak of the tenth cycle. It resembles that of density profiles of positive oxygen ions. The densities of charge species such as electrons and O^- are small in comparison to O_2^+ ions. The value of charge separation q is nearly equal to density of O_2^+ ions. Figure 4 (d) shows slices of density of charge separation at the edges of electrodes at positive peak of the pulsed dc of tenth cycle. The peak of charge separation is very close to the common edge of the powered electrode and

dielectric. Strength and direction of electric field and charge of various species is responsible for this location of densities. Charge separation gives rise to a self-generated electric field through Poisson's Equation. The density decreases sharply with the increase in the distance from the edges of the electrodes or dielectric. Figures 5 (a) and 5(b) show density of various charge species at α = 15° and 45° as a function of z, respectively. These figures give us numerical estimation of variation of density of different charge species along z. Since the discharge is not uniform along the edges of the electrons, variation of charge densities in Figs. 5 (a) and 5(b) are not same.

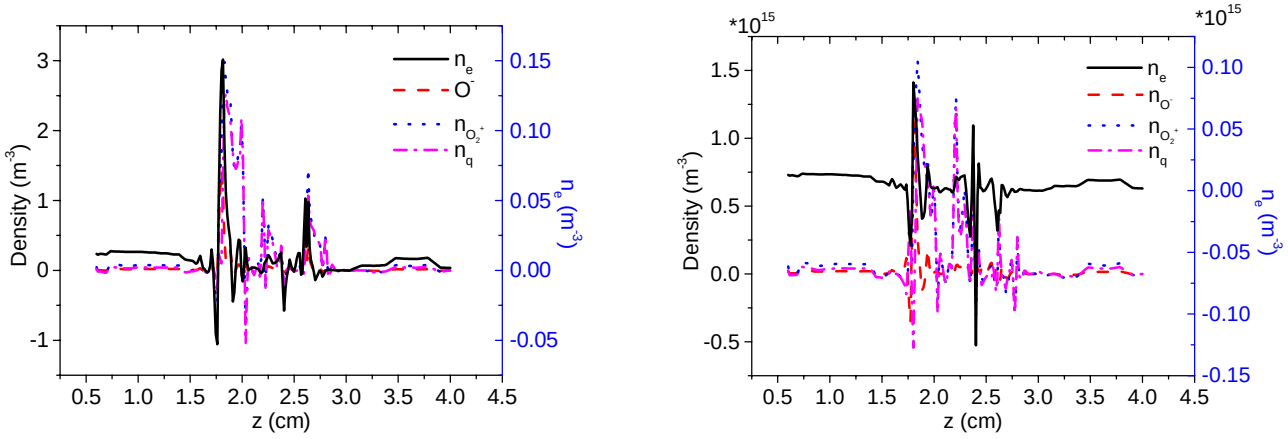

(a) 15° (b) 45°

Figure 5. Density of various charge species at (a) $\alpha = 15^o$ **and (b)** $\alpha = 45^o$

Figure 6 shows spatial distribution of vectors of time average of electrodynamic force $\mathbf{F} = e(n_{O_2^+} - n_e - n_{O^-})\mathbf{E}$ for pulsed dc plasma actuator. The force is strong close to the common edges of dielectric and electrodes due to high electric field and ionization. The direction of time averaged force is in positive z-direction from powered electrode to grounded electrode (from anode to cathode). This may be useful in separation control. The solution will be sensitive to the initial conditions; we have taken only one initial condition which is close to the atmospheric condition. We have investigated the role of negative oxygen ions O_2^- in air chemistry and found that the density of negative oxygen ions O_2^- remains lower than that of positive oxygen ions O_2^+. The positive oxygen ions O_2^+ play more important role compared to O_2^-. These results will be described in another forthcoming study.

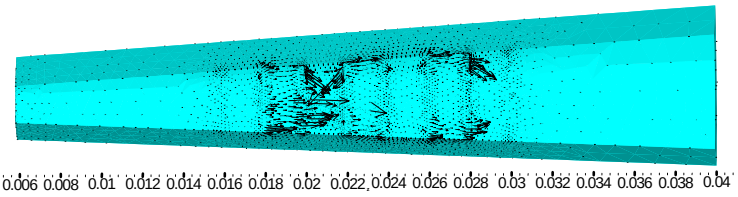

(a) Perspective

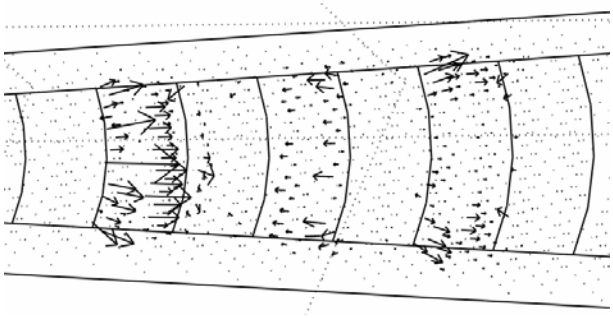

(b) Zoomed in electrode region

Figure 6. Vectors of electrodynamic force $\mathbf{F} = e(n_{O_2^+} - n_e - n_{O^-})\mathbf{E}$.

VI. Conclusions

We have studied a pulsed dc plasma actuator operating in oxygen using a self-consistent multibody modeling of oxygen, plasma and dielectric. Chemistry of formation of different species of oxygen has been taken into account. Species with very high recombination rates and nitrous oxide have been neglected for simplicity. Continuity equations governing densities of electrons, ions and neutral species of nitrogen and oxygen are solved with Poisson's equation using a three-dimensional finite element based formulation of plasma to obtain spatial and temporal profiles of densities of species, and electric field. The electric field and ionization is highest close to the common edges of electrodes and dielectric. Oppositely charged species move in opposite directions due to applied pulsed dc potential which gives rise to charge separation. Poisson's equation governs electric field generated due to charge separation. The density of separated charge $n_q = (n_{O_2^+} - n_e - n_{O^-})$, and the electrodynamic force per volume $\mathbf{F} = e(n_{O_2^+} - n_e - n_{O^-})\mathbf{E}$ have been obtained. The time average of the force shows mostly acceleration in the forward direction (from anode to cathode) above the actuator. This results in a moving wave of plasma over the surface in forward direction which can find application in flow control. A pulsed dc plasma actuator may be used as an alternative to the dielectric barrier discharge plasma actuator.

Acknowledgements

This work was partially supported by the AFOSR grant no. FA9550-07-1-0131 and FA9550-05-1-0074 monitored by LtCol Rhett Jefferies and Dr. John Schmisseur and AFRL research fellowships during the past summers. The authors acknowledge thoughtful discussions with Drs. Datta Gaitonde and Miguel Visbal.

References

[1] O.A.S. Kandil, H. Hazem and C.H. Liu, AIAA-1992-4426 AIAA Atmospheric Flight Mechanics Conference, Hilton Head Island, SC, 1992, Washington, AIAA, 1992, 244.
[2] Celik, Zeki Z. Roberts, Leonard, AIAA-1992-4430 AIAA Atmospheric Flight Mechanics Conference, Hilton Head Island, SC, Washington, AIAA, 1992, 293.
[3] N. Pedreiro, S.M. Rock, Z.Z. Celik and L. Roberts, Journal of Aircraft **35**, 69 (1998).
[4] V. Shalaev, A. Fedorov, N. Malmuth, V. Zharov, and Ivan Shalaev, AIAA 2003-34, 41st Aerospace Sciences Meeting and Exhibit, 6-9 January 2003, Reno, Nevada.
[5] A. A. Maslov, B. Y. Zanin, A. A. Sidorenko, B. V. Postnikov, V. P. Fomichev, A. D. Budovsky, and N. Malmuth, AIAA-2005-400, 43rd AIAA Aerospace Sciences Meeting and Exhibit 2005, Reno, Nevada.
[6] K.P. Singh and S. Roy, J. App. Phys. **101**, 093301 (2007).
[7] J.R. Roth, D.M. Sherman, S.R. Wilkinson, AIAA J., **38,** 7 (2000).
[8] C. L Enloe, T. E. McLaughlin, G. I. Font, and J. W. Baughn, 44th AIAA Aerospace Sciences Meeting and Exhibit, Reno, Nevada, 9 - 12 January 2006 (AIAA, Washington, D.C. 2002), AIAA 2006-166.
[9] T.C. Corke, M.L. Post and D.M. Orlov, Progress in Aerospace Sciences 43 (2007) 193–217.
[10] S.Roy and D.V.Gaitonde, AIAA-2005-0160, 43rd AIAA Aeropsace Sciences Mtg., January 10-13, 2005, Reno NV.
[11] J. Poggie, DC glow discharges: a computational study for flow control applications. AIAA Paper 2005-5303; 2005.
[12] B. Jayaraman, S. Thakur, W. Shyy, Journal of Heat Transfer, **129**, 517 (2007).
[13] G. I. Font, C. L. Enloe, T.E. McLaughlin, and D. Orlov, 45th AIAA Aerospace Sciences Meeting and Exhibit Reno, Nevada 2007 (AIAA, Washington, D.C. 2002), AIAA 2007-188.
[14] J. W. Gregory, C. L. Enloe, G. I. Font, and T. E. McLaughlin, 45th AIAA Aerospace Sciences Meeting and Exhibit Reno, Nevada 2007 (AIAA, Washington, D.C. 2002), AIAA 2007-185.
[15] S. Pavon, J-L Dorier, Ch Hollenstein, P. Ott and P. Leyland, J. Phys. D: Appl. Phys. **40**, 1733 (2007).
[16] C. O. Porter, J. W. Baughn, T. E. McLaughlin, C. L. Enloe, and G. I. Font, 44th AIAA Aerospace Sciences Meeting and Exhibit Reno, Nevada, 9 - 12 January 2006 (AIAA, Washington, D.C. 2002), AIAA 2006-104.
[17] K.P. Singh and S. Roy, J. Appl. Phys., 2007 (in press). M. Visbal, D. Gaitonde and S. Roy, AIAA-2006-3230.
[18] M.P. Patel, T.T. Ng and S. Vasudevan, T.C. Corke, M.L. Post, T.E. McLaughlin and C.F. Suchomel, 45th AIAA Aerospace Sciences Meeting and Exhibit, 8 - 11 January 2007, Reno, NV, AIAA 2007-635.
[19] T. C. Corke, B. Mertz, M. P. Patel, 44th AIAA Aerospace Sciences Meeting and Exhibit Reno, Nevada, 9 - 12 January 2006, (AIAA, Washington, D.C. 2002) AIAA 2006-1208.
[20] K.P. Singh and S. Roy, J. App. Phys. **101**, 123308 (2007).
[21] J. R. Roth and X. Dai, 44th AIAA Aerospace Sciences Meeting and Exhibit, Reno, Nevada, 9 - 12 January 2006 (AIAA, Washington, D.C. 2002), AIAA 2006-1203.
[22] K.P. Singh and S. Roy, Applied Physics Letters, **91**, 081504 (2007).
[23] I. A. Kossyi, A. Yu Kostinsky, A.A. Matveyev and V.P. Silakov, Plasma Sources Sci. Techol., **1**, 207 (1992).
[24] S. Roy and B.P. Pandey, Phys. Plasmas, **9**, 4052 (2002).
[25] H.W. Ellis, et al., Atomic Data Nucl. Data Tables, **17**, 177 (1976).